Article

Design and Analysis of a Novel Floating Docking Mechanism for On-Orbit Refueling

Zhicheng Sun [1,2], Shipeng Li [1,2], Huan Zhang [1,2], Haiming Lei [1,2] and Xiaodong Song [1,2,*]

1   School of Aerospace Engineering, Beijing Institute of Technology, Beijing 100081, China;
    zc_sun@bit.edu.cn (Z.S.); lsp@bit.edu.cn (S.L.); huan_zhang@bit.edu.cn (H.Z.); 3120200053@bit.edu.cn (H.L.)
2   Key Laboratory of Dynamics and Control of Flight Vehicle, Ministry of Education, Beijing 100081, China
*   Correspondence: xd_song@bit.edu.cn

Abstract: The docking mechanism is a key component for on-orbit refueling technology. In this paper, the design and analysis of a novel floating docking mechanism for on-orbit berthing-based refueling is presented. Compared with traditional berthing and docking, the berthing here is high in success rate and low in impact, which is accomplished by stretching out a docking subassembly instead of pulling back the client spacecraft. However, the berthing also has two problems: initial deviations between two spacecraft and an additional force generated by a hard alloy refueling pipe, which both seriously affect the docking operation. Thus, the docking mechanism is designed to have alignment abilities and decrease the additional force as much as possible. Based on the principles above, we introduced spring pins and a helical refueling pipe to design a light, compact, and simple docking mechanism. To further reduce the additional force, we proposed an elliptical-helical pipe and analyzed its mechanical properties. Finally, simulations and experiments were conducted to validate the proposed mechanism. The results show that the proposed mechanism with an elliptical-helical pipe has a high tolerance for linear and angular misalignment and superior dynamic performance during docking.

Keywords: floating docking mechanism; dynamic analysis; elliptical-helical pipe; on-orbit refueling; berthing

1. Introduction

After decades of space flight, an increasing number of satellites have become dead satellites as a result of running out of propellant [1,2]. The traditional solution is to launch new satellites with the same functions to replace dead satellites. At present, an alternative solution is to recover the functioning of dead satellites with on-orbit refueling [3–7], which effectively avoids the problem of dead satellites occupying orbits and extends the life of spacecraft. With the increasing demand for space missions and the complexity of aerospace engineering, on-orbit refueling technology is an urgent requirement among on-orbit service technologies [1,8–11].

Existing methods for on-orbit refueling can be divided into three types [12]: direct filling, propulsion module replacement, and propulsion module addition. Owing to the complexity of the latter two methods, the direct filling method is generally adopted, such as in the International Space Station (ISS) [13] and Orbital Express [14] (technology demonstration).

For direct filling, scholars have performed many studies, such as those on docking systems [15–17], transfer systems [18], docking control [19], and fluid dynamics [20]. In this paper, the docking system is the main focus. Currently, three main categories of docking configurations have been proposed: probe–drogue [13], androgynous [21], and magnetic [22]. The probe–drogue configuration has been the most straightforward docking configuration adopted by large spacecraft since the 1970s [13,21]. In the early 2000s,

Michigan Aerospace Autonomous Microsatellite Docking System II [23], a probe–drogue docking mechanism that can achieve soft docking, was proposed. Then, the Assist project presented a type of probe–drogue docking mechanism [15] that used a pantograph to capture and pull back the target spacecraft in the mid-2010s. Recently, Francesconi et al. presented two probe–drogue docking mechanisms: (1) Autonomous Rendezvous Control and Docking Experiment [24] proposed in 2013, which uses an electromagnet to achieve soft docking and release and uses three locking solenoids to lock the probe–drogue; and (2) a miniature docking mechanism for CubeSats [25] proposed in 2020, which uses photoelectric sensors to judge contact and a rotating tip to lock. As a classical docking configuration, the probe–drogue configuration has been used to this day due to its simple structure.

The main methods for on-orbit joining operations are docking and berthing [13,21]—e.g., Automated Transfer Vehicle and Progress join the ISS by docking—and other refueling/refurbishing automatic modules of the ISS adopt berthing. For docking, two spacecraft dock in a floating state and do not need robotic manipulators to fasten each other. The requirements of the spacecraft navigation system and the impact force of docking are all very high. Moreover, docking has a high failure risk due to floating collisions and bouncing off [25]. For berthing, the client spacecraft berths next to the service spacecraft by robotic manipulators, and the two spacecraft are fastened. Then, the client spacecraft is pulled back to join the service spacecraft or the service spacecraft stretches a docking subassembly to dock with the client spacecraft. The requirements of the robotic manipulators' flexibility and control error are all very high. However, berthing does not exhibit failure risk due to collision and bouncing off, and the impact force is lower than docking due to the low joining velocity [26]. Moreover, compared with the two types of berthing, the impact force of stretching is much lower than that of pulling back due to the lower moving mass. Thus, berthing and joining by stretching a docking subassembly to dock has better application prospects for on-orbit joining operations. The steps are shown in Figure 1 and described as follows:
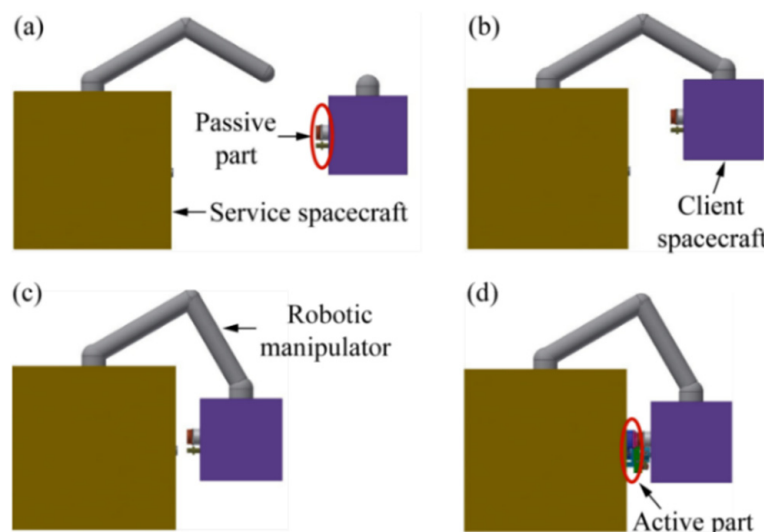

Figure 1. Steps of berthing and joining by stretching: (**a**) approach, (**b**) capture, (**c**) pullback, (**d**) docking.

(a) Approach—the service spacecraft moves toward the client spacecraft using a navigation system until the distance between them is below the maximum capture distance.

(b) Capture—the service spacecraft captures the client spacecraft using a robotic manipulator.

(c) Pullback—the robotic manipulator pulls back and adjusts the attitude of the client spacecraft toward the service spacecraft until the position of the spacecraft falls within

the docking conditions. By this time, the relationship between the service spacecraft and client spacecraft is relatively stationary.

(d) Docking—the active part of the docking mechanism stretches and eventually docks with the passive part to build a propellant transfer pipeline.

For berthing and joining by stretching, the initial position and attitude deviations be-tween the two spacecraft may occur owing to the flexibility and control error of the robotic manipulator. To eliminate these deviations, it is necessary to enable the alignment of the docking mechanism. Moreover, the self-resetting capability of the docking mechanism is also required to return the docking subassembly back to its initial position and attitude after docking and prepare for the next refueling operation.

In addition, a refueling pipe connected to the docking subassembly can be stretched synchronously with a docking subassembly during stretching. Considering the compat-ibility between propellants and the refueling pipe and the high pressure of propellants, the refueling pipe can be generally composed of hard metals, such as titanium or alu-minum alloys, rather than flexible materials [27]. Thus, a nonnegligible additional force on the driving assembly of the refueling pipe should be considered in the design of the docking mechanism. Owing to the single stretching direction of the refueling pipe—that is, the docking direction—a helical configuration is a suitable choice for the refueling pipe to decrease the additional force, as shown in Figure 2. The mechanical properties of helical pipes—especially axial stiffness—need to be researched, which directly affect the additional force.
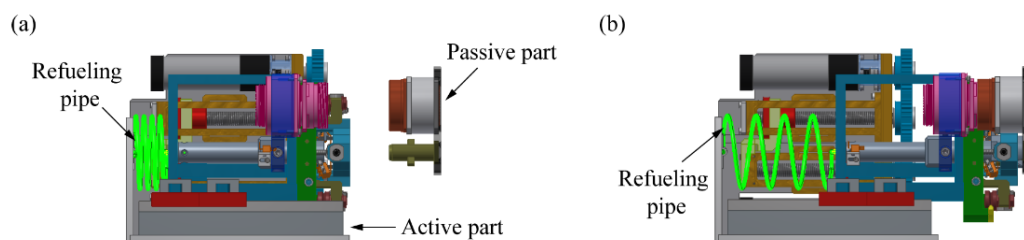

Figure 2. Stretching of a refueling pipe with a helical configuration: (**a**) initial state of compression, (**b**) terminal state of tension.

At present, scholars have mainly focused on circular-helical structures, such as helical springs. Dym [28] derived spring rates by Castigliano's second theorem. Spinella et al. [29] proposed a type of shape memory alloy (SMA) helical spring for an SMA actuator. Jafari et al. [30] derived the exact stiffness matrix of curved beams with nonuniform cross-sections by a direct method. Burns [31] studied the relationship between helical spring compliances and free- and fixed-end rotations. Liu [32] derived the classical formula for a circular-helical spring using an energy-based method. For the on-orbit mechanism, its design space is limited and irregular. An elliptical-helical refueling pipe is more appropriate in compact docking mechanisms than a circular-helical refueling pipe to further decrease the additional force by increasing the envelope of the pipe (decreasing the axial stiffness of the pipe). However, there is almost no research on elliptical-helical structures. For further design and analysis, the axial stiffness of elliptical-helical pipes must be researched, and the expression of the additional force can be derived by analogy with helical springs.

This paper presents a novel floating docking mechanism for on-orbit refueling by berthing. The capacities of the proposed docking mechanism with passive five-DOF alignment for initial deviations and passive self-resetting for multiple refueling are realized using several spring pins. The mechanism is lightweight, simple, and compact in structure based on the probe–drogue configuration. An elliptical-helical pipe configuration with bias loading was proposed to decrease the additional force on the driving subassembly. Then, the influence mechanism of the additional force of the proposed pipe on the docking process is obtained by mechanical analysis, which determines the design of the spring pins and the driving force. The axial stiffness formula of the proposed pipe is derived using an

energy-based method. Finally, simulations and experiments were conducted to evaluate the analyses of the axial stiffness of the elliptical-helical pipe, the contact force, and the tolerance of the mechanism.

The remainder of the paper is organized as follows: Section 2 describes the structure and working principle of the docking mechanism and the process of docking and the mechanical analysis of docking, which determines the elliptical-helical configuration and the significance of the refueling pipe to the docking mechanism. Section 3 describes the building of a model of an elliptical-helical pipe with bias loading and derives the formulas of axial stiffness and maximum stress by the energy-based method and the third strength theory, respectively. Section 4 presents the simulations conducted to investigate the mechanical properties of the pipe, the contact force, the driving force, and the passive alignment ability of the mechanism, as well as the experiments for validating the simulations. The conclusions are presented in Section 5.

2. Description of the Mechanism

As mentioned above, the reference scenario considered during the mechanism design is the steps required for berthing docking when a service satellite has captured a client satellite by a robotic manipulator and is ready to dock. The primary function of the docking mechanism is to establish a fluid transfer pipeline between itself and another satellite. In the design of the mechanism, simplicity and low weight are strongly preferred qualities to decrease the driving force during docking.

The application of the docking mechanism proposed in this paper is not restricted to only one type of satellite. The mechanism can be scaled up or down to adapt to the requirements of different missions. In this study, the design of the docking mechanism aims at the on-orbit refueling by berthing for microsatellites. According to the analyses of Section 1, the design requirements of the docking mechanism can be summarized as follows and the subsequent design need to meet the requirements:

R1—the mechanism shall have five degrees of freedom (DOF) (except in the docking di-rection) alignment abilities to adapt to initial deviations.

R2—the mechanism shall have self-resetting ability for reuse.

R3—the additional force of the refueling pipe needs to be decreased as much as possible to decrease the influences for the docking operation (mainly driving force).

2.1. System Design

The proposed mechanism adopts the traditional probe–drogue configuration with an active drogue and a passive probe. As shown in Figures 3 and 4, the active service part comprises a docking subassembly, passive alignment subassembly, driving subassembly, supporting subassembly, and refueling pipe as the service part. The passive client part consists mainly of a docking subassembly. The basic information of the docking mechanism—i.e., dimension and weight are shown in Table 1—and the direction definitions of each length are shown in Figure 3.

The docking subassembly which is made up of probe and drogue, a pair of electric connectors and a pair of fluidic connectors are used for establishing connection between the service and client part. The supporting subassembly is composed of several supporting structures, playing the role of supporting and fixation. As for the passive alignment subassembly, driving subassembly, and refueling pipe, they are core subassemblies of the proposed mechanism and will be introduced in detail below.

Table 1. Basic information of the docking mechanism.

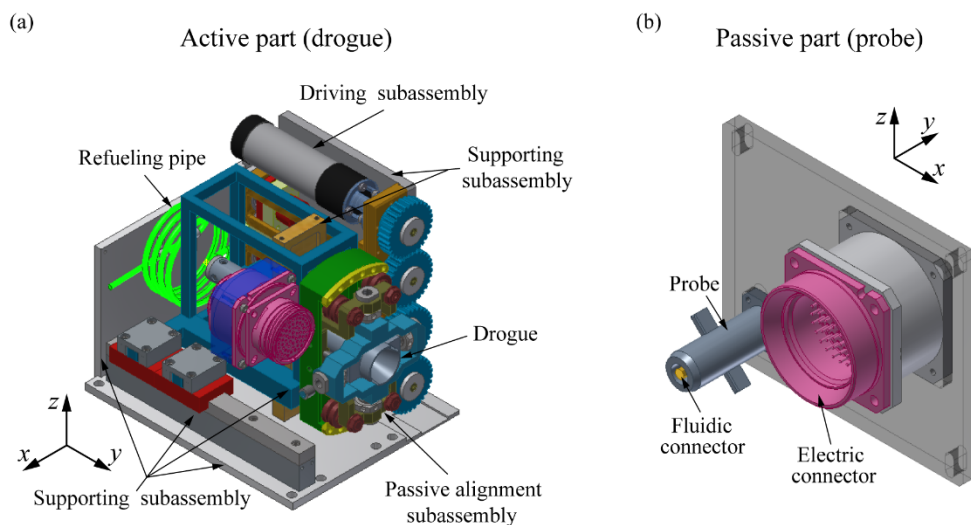|		Dimensions		Weight
	X-Direction	*Y*-Direction	*Z*-Direction	
Active part	174 mm	205 mm	174 mm	4.74 kg
Passive part	119 mm	46 mm	99 mm	0.72 kg

Figure 3. Components of (**a**) the active part and (**b**) the passive part.
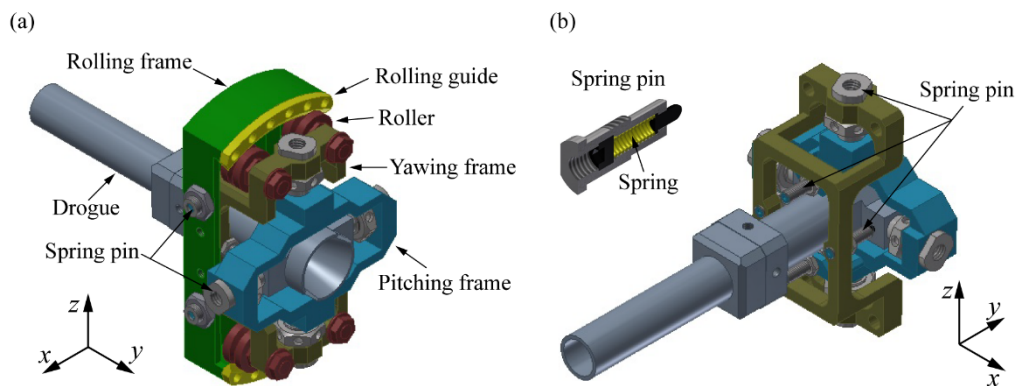

Figure 4. Components of the passive alignment subassembly: (**a**) forward isometric drawing, (**b**) reversed isometric drawing.

2.1.1. Passive Alignment Subassembly

Defining the inertial frame will help describe the adjustment and docking of the mechanism. As shown in Figure 5, the docking direction and roll axis are on the *y*-axis, the horizontal sliding direction and pitch axis are on the *x*-axis, and the vertical sliding direction and yaw axis are along the *z*-axis.

The passive alignment subassembly has the functions of passive alignment and self-resetting in five DOFs, except in the docking direction. The drogue is connected to the passive alignment subassembly to be floating, as shown in Figure 4a. In this way, the synchronous adjustment and docking of the fluidic and electric connectors can be realized.

A rolling frame, yawing frame, pitching frame, and several spring pins are the main structures of the passive alignment subassembly. The drogue and the pitching frame are connected by two preloading spring pins, which become cylindrical pairs so that the drogue can slide and rotate along the *x*-axis to adapt to deviations. The pitching frame and the yawing frame are also connected by two preloading spring pins, such that the pitching frame can slide and rotate along the *z*-axis to adapt to deviations. The yawing frame and the rolling frame are connected by four rollers, which can roll on the rolling guide so that the yawing frame can rotate along the *y*-axis to adapt to deviations.
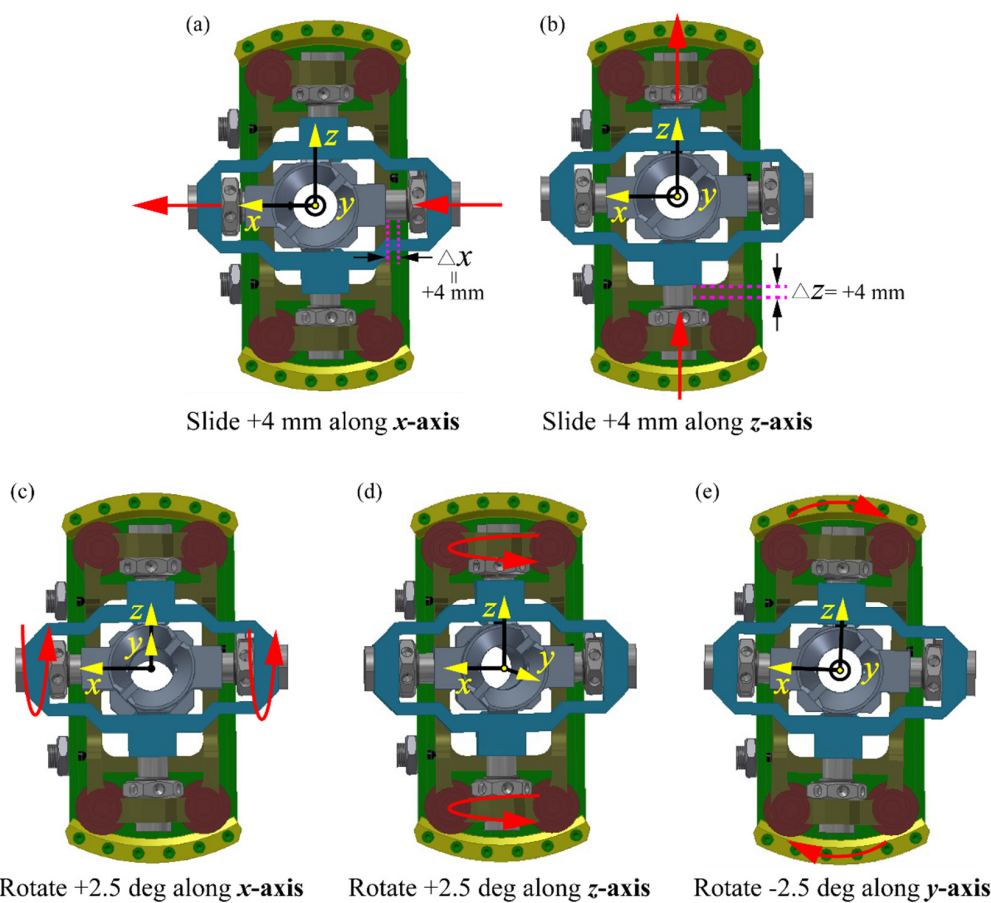
Figure 5. Principle of passive alignment subassembly: (**a**) slide along *x*-axis, (**b**) slide along *z*-axis, (**c**) rotate along *x*-axis (pitch), (**d**) rotate along *z*-axis (yaw), (**e**) rotate along *y*-axis (roll).

A pair of the same preloading spring pins is needed for each DOF to maintain the drogue at an initial state of position zero. During the docking process, the drogue will ad-just passively to adapt to deviations so that the spring force of the spring pin pairs will change (the spring pin along the adjustment direction will be compressed, and the spring force of the pin increases continuously, and another pin is out of contact with the corresponding connecting frame to be inactive), thereby generating a reset force or torque, which will reset automatically after refueling and separating from the docking mechanism. The principle of the passive alignment subassembly is shown in Figure 5. The docking mechanism is floating and reusable because of passive adjustment and self-resetting characteristics, which meet the requirement R1 and R2. The tolerance range of the passive alignment subassembly are shown in Table 2.

Table 2. Tolerance range of the passive alignment subassembly.

Linear Directions		Angular Directions		
X	Z	X	Y	Z
±4 mm	±4 mm	±2.5°	±2.5°	±2.5°

2.1.2. Driving Subassembly

The driving subassembly consists of two identical driving modules. Each module consists of a servo motor (double-winding), two identical spur gears, a trapezoidal screw, and an installation frame, as shown in Figure 6. The servo motor drives the spur gears, stretching the trapezoidal screw which is indirectly connected with the drogue, both of which are attached to the installation frame to form a module, and the trapezoidal screw

locks the driving subassembly by its self-locking. Under normal conditions, the lower driving module works alone and drives the drogue to dock; as the backup, the upper driving module will work and drive lower module one to stretch by part connecting the two modules, thus ensuring the success of docking if the lower driving module does not work. This will increase the reliability of the driving subassembly by four times (as the servo motors are double-winding). The upper installation frame is the fixed end secured by the supporting subassembly. The properties of the driving subassembly are shown in Table 3.
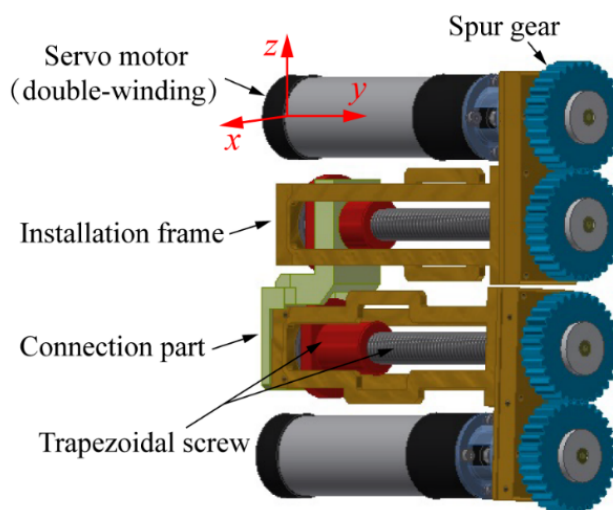

Figure 6. Components of the driving subassembly.

Table 3. Properties of the driving subassembly.

	Dimensions		Power	Driving Force	Travel	Speed	Redundancy
X-Direction	*Y*-Direction	*Z*-Direction					
40 mm	157 mm	166 mm	12 W	1323 N	76 mm	1 mm/s	4

2.1.3. Refueling Pipe

As Figure 2 and 3 show, the refueling pipe is connected to the drogue and stretched along with the docking subassembly under berthing docking; this pipe is generally made of hard metal. Thus, the refueling pipe generates an additional force on the driving subassembly during the docking process, as mentioned in Section 1. A helical configuration for the refueling pipe is an excellent choice for linear tension and compression motion to decrease this additional force. In the context of this paper, the refueling pipe needs to stretch and retract repetitively, meaning that its initial and terminal states must be designed to correspond with compression and tension, respectively, for an equal axial deformation; this is to ensure that the maximum additional force of the two states is equal and the lowest. The additional force generated by the refueling pipe also influences the design of the driving force and spring pins, as explained in Section 2.3. Given the necessary compactness of on-orbit mechanisms, the design space of the refueling pipe is limited and irregular; hence, an elliptical-helical configuration with bias loading is proposed to replace the circular-helical configuration and decrease the additional force, as shown in Figure 7. The expressions of axial stiffness and strength checking of this type of pipe are derived in Section 3.
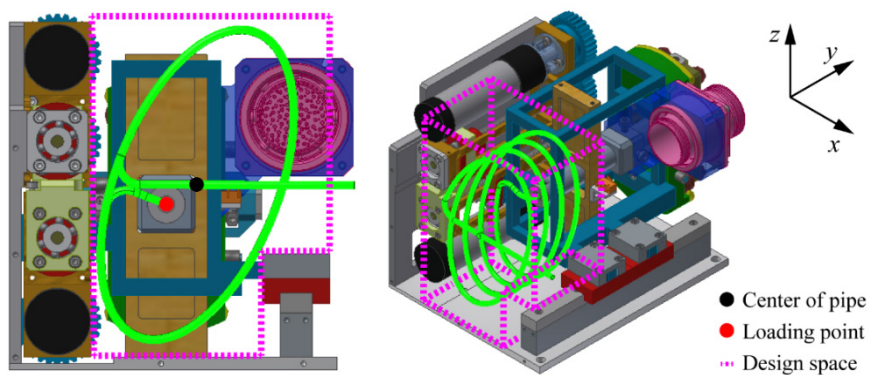
Figure 7. Configuration and design space of the elliptical-helical pipe with bias loading. The red point represents the loading point that connects the drogue and refueling pipe; the yellow point represents the center of the elliptical pipe fixed to the load-carrying plate; the pink dashed line indicates the design space for the refueling pipe, outside of which the envelope of pipe cannot extend.

2.2. Docking Process

As mentioned in Section 1, refueling spacecraft must complete the "approach", "capture", and "pullback" steps before "docking" under the berthing docking. In this section, the sequences of the docking process are designed, as shown in Figure 8.
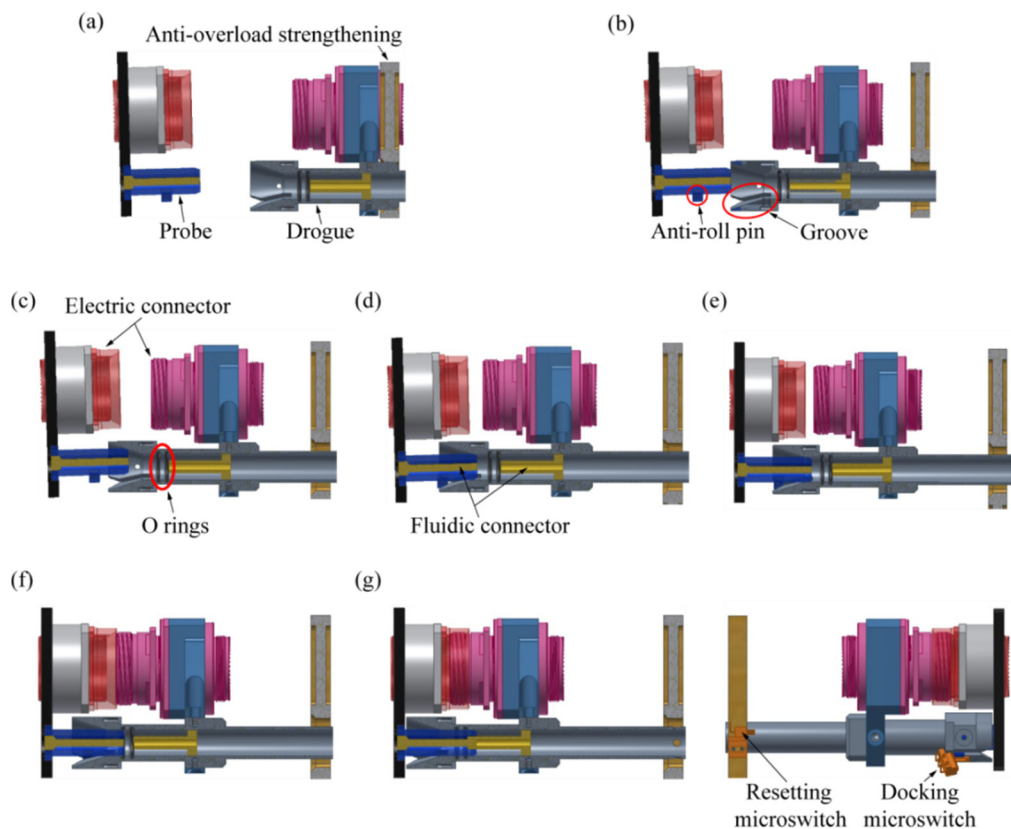

Figure 8. The process of docking: (**a**) initial, (**b**) approach, (**c**) contact and alignment I, (**d**) probe insertion and alignment II, (**e**) pin insertion and alignment III, (**f**) connector docking, (**g**) accomplishing.

The detailed descriptions of the docking process are as follows:

(a)　Initial—the positions of two satellites under the docking conditions in which the probe enters the acceptance range of the drogue; the drogue is still supported by anti-overload strengthening.

(b)   Approach—the system powers on, and the drogue stretches and breaks away from the anti-overload strengthening to be floated; at the same time, the probe is ready to enter into the drogue.

(c)   Contact and alignment I—the drogue stretches continuously to contact with the probe; the contact force adjusts deviations in the X and Z linear directions to achieve the correct alignment.

(d)   Probe insertion and alignment II—the probe is inserted in the hole of the drogue; the contact torque adjusts deviations in the pitch and yaw directions to achieve the correct alignment.

(e)   Pin insertion and alignment III—the anti-roll pins contact the grooves; the contact torque adjusts the deviation in the rolling direction to achieve the correct alignment fully.

(f)   Connector docking—the position and attitude of the electric connector and the fluidic connector are corrected; two connectors are ready to dock.

(g)   Accomplishing—the drogue is inserted continuously until the electric connector and the fluidic connector reach the designed location; the whole docking is accomplished.

So far, the design of the docking mechanism is completed (except for the refueling pipe), and there are some notes need to be paid attention:

(1)   The drogue is not fluid-filled before accomplishing docking.

(2)   Two O-rings are installed in the hole of the drogue and used to prevent fluid leakage when the male fluidic connector breaks away from the female fluidic connector during separation.

(3)   Two docking microswitches are installed beside the two grooves, and the system powers off when the anti-roll pins trigger either of the two microswitches upon the completion of docking; a resetting microswitch is also installed on the anti-overload strengthening and the system powers off when the drogue triggers the microswitch upon the completion of resetting.

(4)   The trapezoidal screw locks the system by its self-locking.

2.3. Mechanical Analysis

In Section 2.1.1, the design requirements R1 and R2 have been met. As another core design criteria, R3 must decrease the driving force during the docking process to decrease the power consumption of the motor and facilitate successful docking. In this section, the mechanical analysis of the system, which was used to guide the design of the driving force, is discussed. The drogue is in a state of low speed and uniform motion throughout the docking process; thus, the docking can be considered as a quasi-static process. The kinematic diagram of the mechanism is shown in Figure 9.
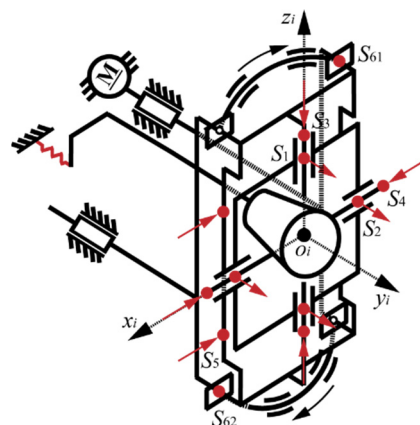

Figure 9. Kinematic diagram of the docking mechanism. The red arrows and the red points represent the preloading spring forces and the points at the corresponding spring pins acted on the drogue, respectively; the 3D model and the principles of the mechanism can be seen in Figures 4 and 5.

From the viewpoint of the docking process, as shown in Figure 8, the mechanical analysis can be divided into three parts:

1. Free stretching

The (a) initial and (b) approach stages of docking comprise the process of free stretching and do not involve contact. The drogue stretches and breaks away from the anti-overload strengthening to float. Owing to the characteristics of the elliptical-helical configuration with bias loading of the refueling pipe, the bias torque generated by the pipe acts on the drogue. To maintain the initial attitude of the drogue, the corresponding spring pins must have sufficient preloading to compete with the bias loading of the pipe, or the drogue will slant, and the initial deviations will increase, resulting in failed docking. The free-body diagram of the initial floated state is shown in Figure 10a, and the preloading conditions of the corresponding spring pins can be obtained by the following equation:

$$
\begin{cases}
F_{is1} > -\dfrac{F_r \cdot z_r + \mu_s \cdot F_r \cdot r_{s24}}{z_{s1}} \\
F_{is2} > -\dfrac{F_r \cdot x_r - \mu_s \cdot F_r \cdot r_{s13}}{x_{s2}}
\end{cases}
\tag{1}
$$

where F_{is1} and F_{is2} are the preloading of the resetting spring pins for pitching and yawing respectively, F_r is the axial force of the refueling pipe, μ_s is the friction coefficient of the spring pins and frame, r_s is the radius of spring pins, S_1 is the point at which the resetting pitching spring pin acts on the yawing spring pin, S_2 is the point at which the resetting yawing spring pin acts on the pitching spring pin, R is the point at which the refueling pipe acts on the drogue, $S_1 S_3$ and $S_2 S_4$ represent the yawing and pitching spin axes respectively, and x and z represent the distance between a point corresponding to the subscript and another axis; for instance, z_{s1} represents the distance between point S_1 and x_r-axis.
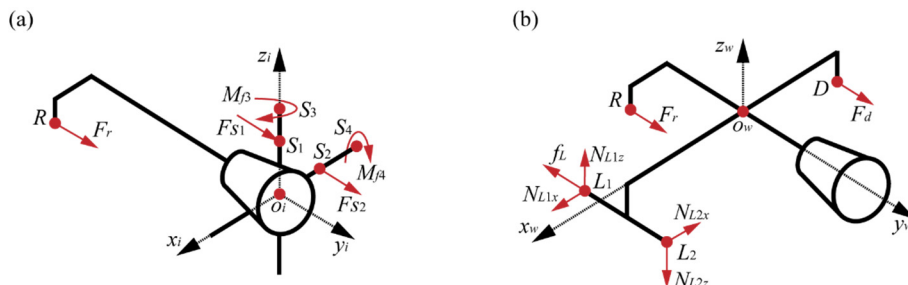
(a)   (b)

Figure 10. Free-body diagram of (**a**) the preloading condition of spring pins and (**b**) free stretching.

Then, the drogue stretches at a constant, continuous speed until it contacts the probe. The servo motor generates the driving force of the drogue to compete with the resistance forces, including the axial force of the refueling pipe and the friction of the linear guide-way. The spur gears and trapezoidal screw of the driving subassembly lead to an efficiency loss of the driving force. The free-body diagram of the free stretching process is shown in Figure 10b, and the driving force can be obtained using the following equation:

$$
F_d = \frac{1}{\eta_g \cdot \eta_s} \cdot \frac{\mu_L (x_{L1} - z_{L1} - x_r - z_r) + y_{L1}}{\mu_L(-x_{L1} + z_{L1} + x_d + z_d) - y_{L1}} \cdot F_r
\tag{2}
$$

where F_d is the driving force, η_g and η_s are the efficiency of the spur gears and trapezoidal screw, μ_L and f_L are the friction coefficient and friction of the linear guideway, D is the point of action of the driving force, L_1 and L_2 are the endpoints of the linear guideway, N_{L1x} and N_{L2x} are the supporting forces of points L_1 and L_2 along x_w-axis, and N_{L1z} and N_{L2z} are the supporting forces of points L_1 and L_2 along z_w-axis.

2   Contact and alignment

The drogue and probe must then make contact and self-align by completing steps (c), contact and alignment I; (d), probe insertion and alignment II; and (e), pin insertion

and alignment III. Through this process, the drogue makes contact with the probe and must compete with the spring force of the pipe, the friction of the linear guideway and linear spring pins, and the contact force is affected by the spring force of the spring pins. Considering step (c) as an example to summarize the factors influencing the driving force, a free-body diagram of this step is shown in Figure 11, and the driving force can be obtained by the following equation:

$$\begin{cases} F_d - F_r - f_L = N_{cy} + f_{cy} \\ F_{s3} + f_{s13} = N_{cz} - f_{cz} \\ F_{s4} + f_{s24} = N_{cx} - f_{cx} \end{cases} \tag{3}$$

where N_c and f_c are the component forces of the contact force, representing the normal contact force and the tangential contact force, respectively, acting on the drogue through the probe. The subscripts represent the direction of the component force, representing the component force of N_c along the y-axis, and F_s and f_s are the spring force and the friction of the linear spring pins along the corresponding axis acting on the drogue.
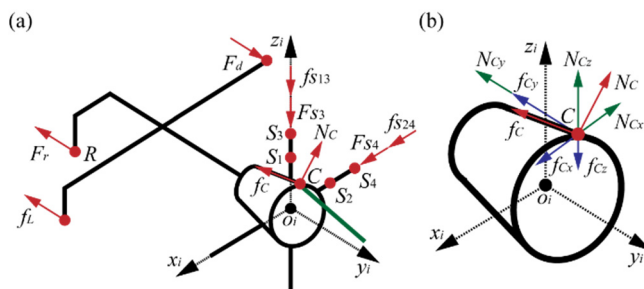

Figure 11. Free-body diagram of "contact and alignment I": (**a**) the mechanical analysis of the drogue (the green line represents the probe), (**b**) the orthogonal decomposition of the contact forces.

In step (c), the contact force is related to the spring forces of the two linear spring pins. Similarly, the contact force of process (d) is related to the spring forces of the yaw and pitch spring pins and (e) to that of the roll spring pins; thus, the driving force is determined by the contact force. Therefore, decreasing the spring force (preloading and axial stiffness) of the spring pins decreases the driving force.

3. Accomplishing and resetting

After the process of contact and alignment, the drogue has achieved the correct alignments and is ready for step (f) and connector docking. By this time, the spring pins have reached the maximum amount of compression, and the spring forces compressed the drogue on the probe. Thus, the driving force of process (*f*) can be obtained using the following equation:

$$F_d = F_r + f_L + f_{dp} + F_{ie} \tag{4}$$

where f_{dp} is the friction between the drogue and probe, and F_{ie} is the insertion and extraction forces of the fluidic and electric connectors.

After process (f), the docking process is complete, and the mechanism refuels the client craft. The drogue will separate from the probe after refueling, and to ensure that the docking mechanism can be reused, the preloading of the spring pins must be high enough to reset the drogue. Considering the extreme case, the drogue does not reset until it completely breaks away from the probe. The preloading of spring pins must be greater than the friction in the corresponding joints caused by the compression of the helical refueling pipe and the precompression caused by machining accuracy and assembly errors, as shown in Figure 12. Thus, the resetting conditions of the corresponding spring pins can be obtained using the following equation:

$$F_{si} > f_{ri} + f_{mi}, i = 1 \ldots 5 \tag{5}$$

where i represents the five joints for alignment, F_s is the preloading of the spring pin, f_r is the friction generated by the compression of the refueling pipe acting on the kinematic pair, and f_m is the friction of the kinematic pair caused by machining accuracy and assembly errors.
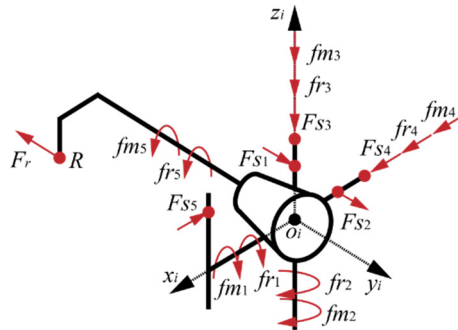

Figure 12. Free-body diagram of the resetting conditions of the drogue.

The conclusions reached through the mechanical analysis of each process are summarized below:

(1) The spring force of the helical refueling pipe exists throughout the docking process and cannot be ignored as one of the resistances of the driving force.

(2) The driving force is related to the contact force, which is related to the preloading and axial stiffness of the spring pins.

(3) The preloading and axial stiffness designs of the spring pins are based on the preloading condition (Equation (1)) and the resetting condition (Equation (5)), which are related to the axial force of the helical refueling pipe.

(4) As a precondition for satisfying the preloading and resetting conditions, the axial stiffness of the spring pins should be as low as possible to prevent an increased con-tact force.

In summary, decreasing the axial force of the helical refueling pipe can significantly decrease the driving force of the docking mechanism. Thus, the structural and mechanical property design of helical refueling pipes is a significant area of research. In addition, the design space for the refueling pipe is irregular because of the compactness of the on-orbit mechanisms. Therefore, an elliptical-helical pipe with bias loading may be a better choice for the refueling pipe, as its envelope is larger, which means the axial stiffness is lower, and the mechanical properties of the pipe are analyzed in Section 3.

3. Mechanical Properties of an Elliptical-Helical Pipe

An elliptical-helical pipe with bias loading has a lower axial stiffness than a circular-helical pipe traditionally as a refueling pipe, which is beneficial for the driving force. However, there is no derivation of the mechanical properties of elliptical-helical pipes. In this section, the expression of the axial stiffness and the strength checking of elliptical-helical pipes are derived to guide the design of this type of pipe.

3.1. Axial Stiffness of an Elliptical-Helical Pipe

An energy-based method [32] is used to derive the axial stiffness of an elliptical-helical pipe with bias loading. According to the law of energy conservation, when a helical structure is telescoped, the work W of an external force F is transferred into the strain energy V_ε of the structure, as shown in Equation (6):

$$W = \frac{1}{2} \cdot F \cdot \lambda = V_\varepsilon \Rightarrow F = \frac{2V_\varepsilon}{\lambda} \tag{6}$$

where λ is the axial deformation of the helical structure under the external force F.

By deriving the formula for the strain energy V_ε and substituting it into Equation (6), the equation relating the net external force F and the axial deformation λ can be

obtained; thus, the axial stiffness of the helical structure can be expressed as follows: As an inherent attribute, the value of the stiffness cannot be influenced by changing the value and position of the external force when the geometrical parameters and material of the structure are confirmed. The external force only influences the stress distribution of the helical structure. Thus, the study of the axial stiffness of an elliptical-helical pipe with bias loading is equivalent to the study of the axial stiffness of an elliptical-helical pipe with center loading. The condition of bias loading can be considered when determining the strength of the pipe. The design space for the refueling pipe is minimal because of the compactness required for an on-orbit refueling mechanism. The pitch angle of the pipe is generally less than 5°, so its influence can be neglected [32]. The configuration of the refueling pipe proposed in this study is shown in Figure 13.
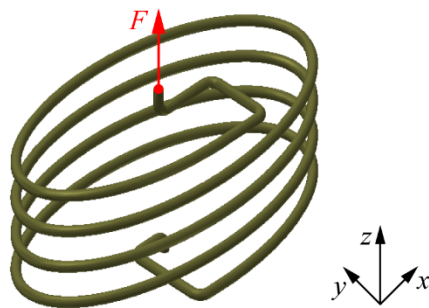

Figure 13. Configuration of the refueling pipe. The red point represents the connecting point of the drogue and the refueling pipe, which is subjected to the force F along the z-axis.

For the helical pipe, the strain energies of each coil are the same. Therefore, the strain energy V_ε of the entire pipe can be derived by multiplying the number of coils and the strain energy of one coil (3D transformed into 2D). To obtain the strain energy V_ε, the geometrical relationship of the elliptical envelope of the pipe is first analyzed. The relationship between O and Q from the top view of the elliptical-helical pipe and the coordinate system is shown in Figure 14. Point O is the center of the elliptical envelope, which is subjected to a force F along the positive direction of the z-axis. Point Q is an arbitrary point on an elliptical envelope.
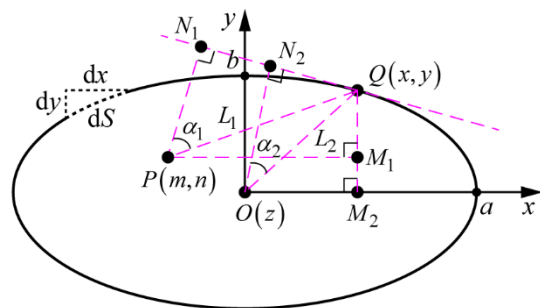

Figure 14. Relationship of OQ and PQ on the elliptical envelope.

As shown in Figure 14, the elliptical envelope equation can be obtained as follows:

$$\frac{x^2}{a^2} + \frac{y^2}{b^2} = 1 \text{ and } \begin{cases} x = a \cdot \cos \varphi \\ y = b \cdot \sin \varphi \end{cases} \tag{7}$$

where a is the semi-major axis of the ellipse, and b is the semi-minor axis of the ellipse.

The included angle $\angle N_2OQ$ formed by line ON_2, which connects point N_2 on arbitrary point Q's tangent line to the ellipse and the ellipse center O. Line OQ, which connects the ellipse center O and arbitrary point Q, can be obtained, which is denoted as α_2:

$$\alpha_2 = \arctan\left(\frac{a^2}{b^2} \cdot \frac{y}{x}\right) - \arctan\left(\frac{y}{x}\right) \tag{8}$$

Through the analysis above, the geometrical relationship of the ellipse center O to an arbitrary point Q can be obtained. The formula of torque T and bending moment M's action on the arbitrary point Q of the ellipse can therefore be expressed as follows:

$$T = F \cdot \sqrt{x^2 + y^2} \cdot |\cos \alpha_2| \tag{9}$$

$$M = F \cdot \sqrt{x^2 + y^2} \cdot |\sin \alpha_2| \tag{10}$$

The work done by an external force on an elliptical-helical pipe is converted into strain energy, which can be derived using the infinitesimal method (IM):

$$V_\varepsilon = V_{\varepsilon T} + V_{\varepsilon B} \tag{11}$$

where $V_{\varepsilon T}$ and $V_{\varepsilon B}$ are the strain energies caused by torque T and bending moment M, respectively.

As shown in Figure 15, the $V_{\varepsilon T}$ can be obtained by IM:

$$V_{\varepsilon T} = N \cdot \int_V v_T dV_T \tag{12}$$

where N and V are the number of active coils and the pipe volume, respectively, dV_T is the volume of the infinitesimal influenced by torque T, and v_T is the density of strain energy caused by torque T.
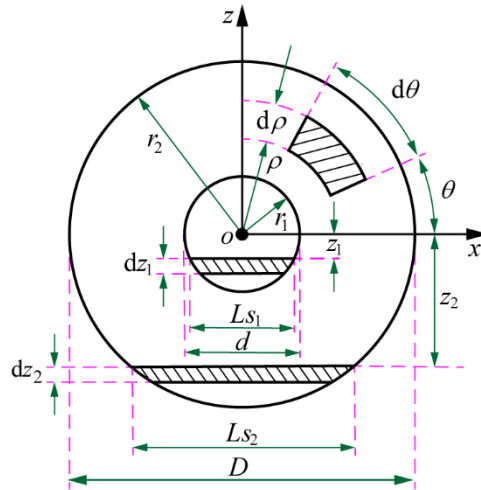

Figure 15. Infinitesimal area dA_T (the curved shadow) and dA_B (the straight shadow) of the refueling pipe section subjected to torque T and bending moment M, respectively.

According to the mechanics of the materials [32], v_T can be obtained using the following equation:

$$v_T = \frac{512}{G} \cdot \left[\frac{T\rho}{\pi(D^4 - d^4)}\right]^2 \tag{13}$$

where G is the shear modulus of the material, ρ is the distance from the infinitesimal to the original point O, and d and D are the internal and external diameters of the refueling pipe, respectively.

According to Figures 14 and 15, dV_T can be obtained as follows:

$$dV_T = \rho \cdot d\theta \cdot d\rho \cdot \sqrt{(a\sin\varphi)^2 + (b\cos\varphi)^2} \cdot d\varphi \tag{14}$$

where $d\theta$ is the included angle of the infinitesimal.

Substituting Equations (13) and (14) into Equation (12), $V_{\varepsilon T}$ can be obtained as:

$$V_{\varepsilon T} = \frac{64Nab^2F^2}{\pi G(D^4 - d^4)} \cdot \text{EllipticK}(\sqrt{\frac{(a^2 - b^2)}{a^2}}) \tag{15}$$

where EllipticK is the first kind of complete elliptic integral.

Similarly, as shown in Figure 15, $V_{\varepsilon B}$ can be obtained by the IM:

$$V_{\varepsilon B} = N \cdot \int_V v_B dV_B \tag{16}$$

where dV_B is the volume of the infinitesimal influenced by M, and v_B is the strain energy density caused by the bending moment M.

According to the mechanics of materials [32], v_B can be obtained as follows:

$$v_B = \frac{2048}{E} \cdot \left[\frac{Mz}{\pi(D^4 - d^4)}\right]^2 \tag{17}$$

where E is the elastic modulus of the material, and z is the distance of the infinitesimal from the center.

According to Figures 14 and 15, dV_B can be obtained using the following equation:

$$dV_B = 2\sqrt{r^2 - z^2} \cdot dz \cdot \sqrt{(a\sin\varphi)^2 + (b\cos\varphi)^2} \cdot d\varphi \tag{18}$$

where dz is the length of the infinitesimal along the z-axis, and r is the radius of the pipe, including the internal radius r_1 and external radius r_2.

Substituting Equations (17) and (18) into Equation (16), $V_{\varepsilon B}$ can be obtained as:

$$V_{\varepsilon B} = \frac{128NF^2}{3\pi E(D^4 - d^4)} \cdot \left[-2ab^2\text{EllipticK}(\sqrt{\frac{(a^2 - b^2)}{a^2}}) + a\left(a^2 + b^2\right)\text{EllipticE}(\sqrt{\frac{(a^2 - b^2)}{a^2}})\right] \tag{19}$$

where EllipticE is the second kind of complete elliptic integral.

Substituting Equations (15) and (19) into Equations (6) and (11), the axial stiffness of the elliptical-helical pipe K can be obtained as:

$$K = \frac{3\pi GE(D^4 - d^4)}{128N\left[(3E - 4G)ab^2\text{EllipticK}\left(\sqrt{\frac{a^2 - b^2}{a^2}}\right) + 2Ga(a^2 + b^2)\text{EllipticE}\left(\sqrt{\frac{a^2 - b^2}{a^2}}\right)\right]} \tag{20}$$

When $a = b = R$, the elliptical pipe degrades into a circular pipe. Equation (20) can be rewritten as follows:

$$K = \frac{G(D^4 - d^4)}{64NR^3} \tag{21}$$

where R is the radius of the circular pipe envelope.

3.2. Strength Checking of an Elliptical-Helical Pipe

Except for the axial stiffness, the maximum stress of the refueling pipe, which cannot exceed the allowable stress on the material, is another important mechanical property of the pipe to be analyzed. In this section, the bending moment M' and torque T' acting on point Q of the pipe are derived. Using the third strength theory as the strength-checking formula and substituting M' and T' into it, the formula can be obtained.

The relationship between P and Q from the top view of the elliptical-helical pipe is shown in Figure 14. Point P is the loading position, which is subjected to a force F along the positive direction of the z-axis. Point Q is an arbitrary point on an elliptical envelope.

According to Figure 14, Equations (22)–(25) can be obtained as follows:

The included angle $\angle N_1 PQ$ formed by line PN_1, which connects point N_1 on the arbitrary point Q's tangent line to the ellipse to the loading position P. Line PQ, which connects P to an arbitrary point Q, can be obtained, which is denoted as α_1:

$$\alpha_1 = \arctan\left(\frac{a^2}{b^2} \cdot \frac{y}{x}\right) - \arctan\left(\frac{y-n}{x-m}\right) \tag{22}$$

where (m, n) is the coordinate of the loading position P.

The distance between the loading position P and arbitrary point Q on the ellipse is denoted as L_1.

$$L_1 = \sqrt{(x-m)^2 + (y-n)^2} \tag{23}$$

The formula of torque T' and bending moment M''s action on the arbitrary point Q of the ellipse by the force F in the loading position P can be expressed as follows:

$$T' = F \cdot L_1 \cdot |\cos\alpha_1| \tag{24}$$

$$M' = F \cdot L_1 \cdot |\sin\alpha_1| \tag{25}$$

The third strength theory [32] is used as the strength-checking formula by combining the formula with Equations (24) and (25), the expression of strength checking can be obtained using the equation below:

$$\sigma_{max} = \frac{32FL_{1max}}{\pi D^3(1-\alpha^4)} \leq [\sigma], \text{ where } \alpha = \frac{d}{D} \tag{26}$$

where $[\sigma]$ is the allowable stress of the material.

The expression of L_{1max} is obtained by combining Equations (7) and (23) to find the point Q_{max} corresponding to L_{1max}. The derivative of $(L_1)^2$ is calculated by ordering the derivative of $(L_1)^2$ equal to zero and calculating its square to obtain the x-coordinates x of the point Q_{max}, as shown in the following equation:

$$\left(a^2 - b^2\right)^2 x^4 - 2a^2 m\left(a^2 - b^2\right)x^3 - a^2\left[\left(a^2 - b^2\right)^2 - a^2 m^2 - b^2 n^2\right]x^2 + 2a^4 m\left(a^2 - b^2\right)x - a^6 m^2 = 0 \tag{27}$$

Equation (27) is a quartic equation with one variable, x. The results of Equation (27) consist of two positive real roots and two negative real roots. The selection of x depends on m, in that their signs are opposite, and x then chooses the larger value in the left two values, which is the correct result. Then, by substituting x into Equation (7). Similarly, the signs of y and n are opposite, and the y-coordinates y of the point Q_{max} can be obtained. Subsequently, L_{1max} can be obtained by substituting x and y into Equation (23). Finally, by substituting L_{1max} in Equation (26), the strength of the pipe is checked. This completes the analysis of the mechanical properties of the elliptical-helical refueling pipe, which can guide the design of such pipes.

4. Analysis and Discussion of Simulations and Experiments

After the design and mechanical analyses of the mechanism, three types of numerical simulations are performed in this section to investigate the static behavior of the refueling pipe and the kinematic and dynamic behavior of the docking mechanism: (1) a static simulation of the mechanical properties of the refueling pipe, (2) a kinematic simulation of the tolerance range of the docking mechanism, and (3) a dynamic simulation of the contact force and driving force of the docking mechanism. Corresponding experiments are per-formed to validate the simulations.

4.1. Static Analysis of a Refueling Pipe

The static simulation and experiment on the mechanical properties of the refueling pipe are performed in this section to verify the accuracy of the analytical solution (Equations (20) and (26)).

An ABAQUS simulation was performed for comparison with theoretical results. The parameters of the numerical validation model of the elliptical-helical pipe with bias loading are listed in Table 4.

Table 4. Parameters of the numerical validation model of the elliptical-helical pipe with bias loading.

Definition	Symbol	Value
Semi-major axis of envelope/mm	a	70
Semi-minor axis of envelope/mm	b	35
External diameter of pipe/mm	D	4
Inner diameter of pipe/mm	d	2.4
Number of active coils of pipe	N	4
Pitch angle of pipe/°	β	2
Position of loading/mm	$P\,(m, n)$	$(-10, -7)$
Permissible stress of TC4/MPa	$[\sigma]$	825
Elasticity modulus of TC4/GPa	E	110
Shear modulus of TC4/GPa	G	41
External force/N	F	49

By substituting the parameters into Equations (20) and (26), the theoretical results of the numerical validation model can be obtained as follows:

$$\begin{cases} K_t = 0.2482\,\text{N/mm} \ \Rightarrow \lambda_t = 40.3\,\text{mm} \\ \sigma_{\text{max t}} = 147.0\,\text{MPa} \end{cases} \tag{28}$$

where the subscript 't' refers to the theoretical result.

The axial deformation of the helical part is denoted as λ_t. However, in actual conditions, each end of the pipe is connected to the drogue and propellant tank. As shown in Figure 13, these connecting parts resemble cantilever beams whose deformation can be calculated by the mechanics of materials [32]. For the numerical validation model in Table 3, the deformation of the connecting part is 0.25 mm.

The third strength theory is used as the strength-checking formula in this study, but the fourth strength theory is used in ABAQUS. To compare the strength-checking result with ABAQUS $\sigma_{\text{max t}}$ is calculated again by the fourth strength theory (0.866 times as much as the third strength theory), which is 127.3 MPa.

Thus, Equation (28) is updated to create Equation (29):

$$\begin{cases} K_t = 0.2466\,\text{N/mm} \ \Rightarrow \lambda_t = 40.3 + 0.25 = 40.55\,\text{mm} \\ \sigma_{\text{max t}} = 127.3\,\text{MPa} \end{cases} \tag{29}$$

When ABAQUS is used to simulate the model above, the results slightly approach the theoretical results as the number of finite elements increases, as shown in Figure 16. Finally, the results converge when the number of finite elements is more than 1.2×10^5 and

the converged results of simulation are shown in Figure 17. The values of λ_A and K_A are obtained using the following equation:

$$\begin{cases} \lambda_A = 41.00 \text{ mm} \Rightarrow K_A = 0.2439 \text{ N/mm} \\ \sigma_{\text{max A}} = 126.5 \text{ MPa} \end{cases} \tag{30}$$
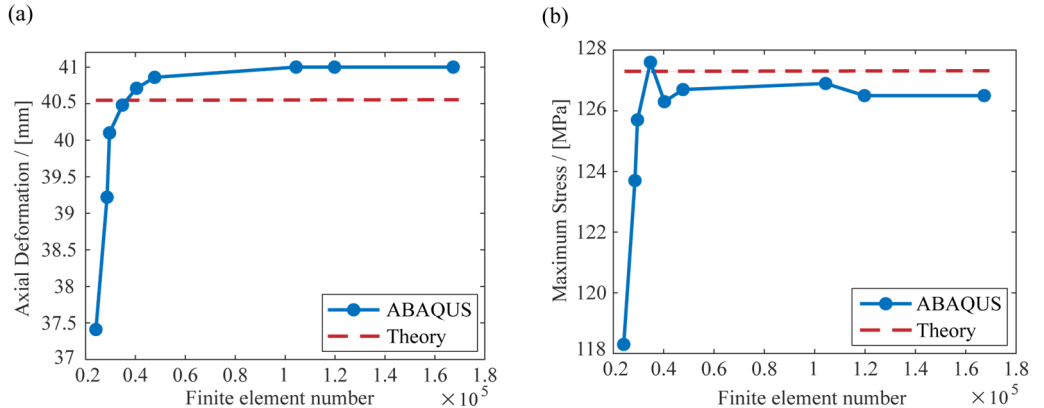
where subscript 'A' refers to the ABAQUS result.

Figure 16. Comparisons of (**a**) axial deformation and (**b**) maximum stress between results of ABAQUS and theory by changing the number of finite elements. Red dashed line represents the theoretical result; the blue line connecting blue points represents the ABAQUS result.
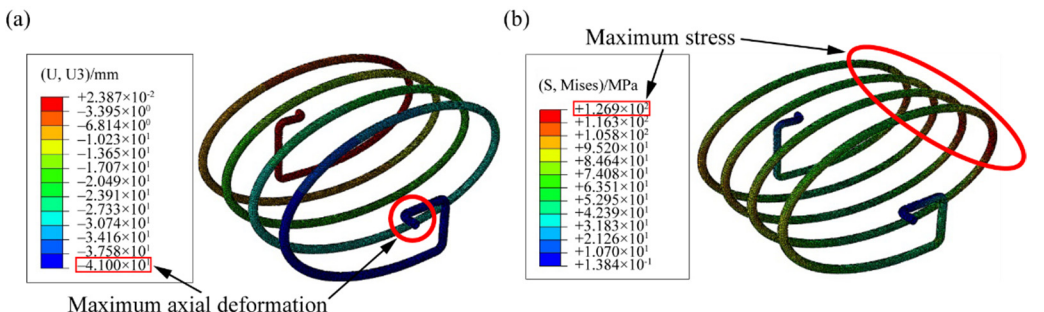

Figure 17. The converged results of simulation: (**a**) axial deformation and (**b**) maximum stress.

Compared with the theoretical results and simulation results—i.e., Equations (29) and (30)—the relative errors of the axial deformation and maximum stress are less than 1.2% and 0.6%, respectively, which verifies the validity and accuracy of the analytical solution. Because the effects of the pitch angle are neglected in the present study, the theoretical axial deformation result is lower than the ABAQUS result.

Then, an experiment was performed to validate the theoretical results and the simulation of the axial stiffness of the pipe. As shown in Figure 18, the experimental system consists of foundation support, an air-bearing linear guideway, a weight, and a refueling pipe. Because of the bias loading characteristic of the refueling pipe, an air-bearing linear guideway is used in the experiment to keep the pipe moving in a straight line to test the axial stiffness, and the low friction coefficient of the air-bearing linear guideway does not generate additional resistance, which will not affect the accuracy of the experiment.
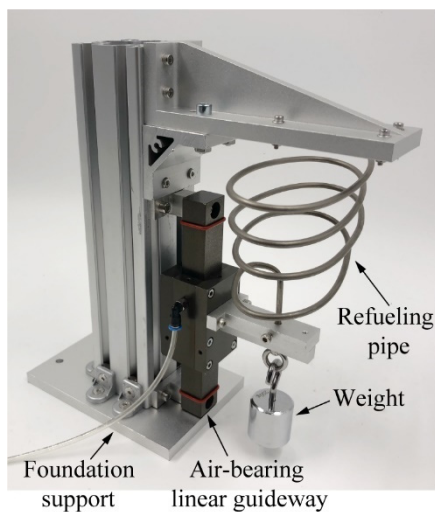
Figure 18. Experiment for axial stiffness testing of the elliptical-helical pipe with bias loading.

By hanging weight underneath the pipe (as in the simulation), the elongation λ_e can be tested, and the axial stiffness of the refueling pipe K_e: $K_e = 0.2579$ N/mm. Comparing the experimental and theoretical results, the relative error of the axial stiffness is less than 4.4%, which validates the accuracy of the theoretical formula (Equation (20)). Thus, the theoretical formulas can guide the design of an elliptical-helical pipe with bias loading.

4.2. Kinematic Analysis of the Docking Mechanism

A kinematic simulation and experiment on the tolerance range of the docking mechanism are performed in this section to verify R1 and R2.

First, a RecurDyn simulation was performed. The 3D model is directly imported from the model reported in Figure 3, and the kinematic diagram of the docking mechanism is shown in Figure 9. The probe is fixed, and the servo motor drives the drogue with a five-DOF adjustment to dock with the probe. By changing the initial state (the linear and angular misalignments between the probe and the drogue), the tolerance range of the docking mechanism can be ascertained by simulation.

An experiment was then performed to validate the simulation results of the tolerance range. As shown in Figure 19, the experimental system consists of a docking mechanism (including an active part and a passive part), foundation support, an adjustment device with five DOFs (except in the docking direction), a six-component force sensor used for the dynamics experiment in the next section, and a control box. The five-DOF adjustment device, whose accuracy is 0.01 mm and 0.01°, is decoupled so that it can adjust for each DOF alone. Through the adjustment device, the experiment can recreate the working conditions of the simulation to validate the results of the tolerance range of the docking mechanism.

Using this design, the tolerance range of the docking mechanism was estimated. To validate the theoretical range, working conditions must be chosen around the boundaries of the theoretical range. In addition, by considering the central symmetry of the passive alignment subassembly, a quarter of the working conditions are sufficient to validate the range. Thus, nine types of working conditions were tested in the simulations and experiments, as shown in Figure 20. In presenting the results, the horizontal and vertical axes represent two linear and three angular deviations, respectively. For example, point $(-2, -1)$ reveals that the initial deviations between the drogue and the probe are $(-2$ mm, -2 mm, $-1°$, $-1°$, $-1°)$; in the simulations and experiments reproducing these deviations, docking is successful. The kinematic simulations and experiments verified the validity of the estimated tolerance range (± 4 mm on two linear directions and $\pm 2.5°$ on three angular directions).

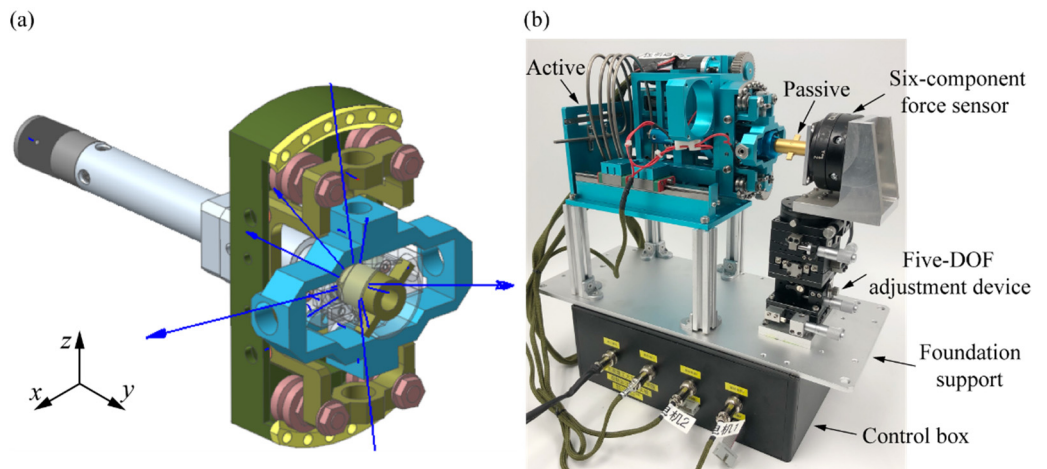**Figure 19.** Components of the kinematic/dynamic (**a**) simulation system (**b**) experiment system.
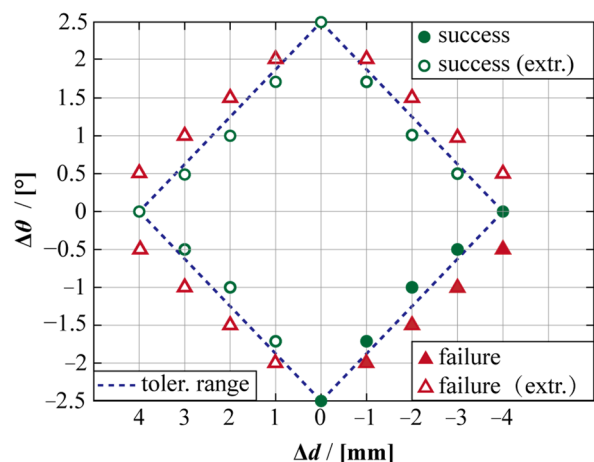

Figure 20. Kinematic results of tolerance range of the docking mechanism. Δd represents the two linear deviations, $\Delta \theta$ represents the three angular deviations, the dashed line represents the estimate tolerance range, the circles represent successful docking, and the triangles represent failed docking. Empty symbols are considered according to the central symmetry of structure to be extrapolated results.

4.3. Dynamics Analysis of the Docking Mechanism

A dynamic simulation and experiment on the contact force and driving force of the docking mechanism are performed in this section to verify the positive influence of the elliptical-helical refueling pipe on the docking mechanism with bias loading. The simulation and experiment took no account of gravity.

As discussed in Section 2.3, the driving force is determined by the preloading and axial stiffness of the spring pins, and these characteristics of the spring pins are determined by the spring force of the refueling pipe. Therefore, decreasing the spring force of the refueling pipe can significantly decrease the driving force of the docking mechanism. A helical structure can decrease the resistance further for motion in a straight line, so a circular-helical pipe with center loading is proposed for such an application. By considering the loading point and the design space, as shown in Figure 7, three other types of analogical pipes can be proposed: a circular-helical pipe with bias loading, elliptical-helical pipe with center loading, and elliptical-helical pipe with bias loading, as shown in Figure 21. In addition, the preloading condition (Equation (1)) and the resetting condition (Equation (5)), each type of pipe can be matched with a set of spring pins, as shown in Tables 5 and 6.
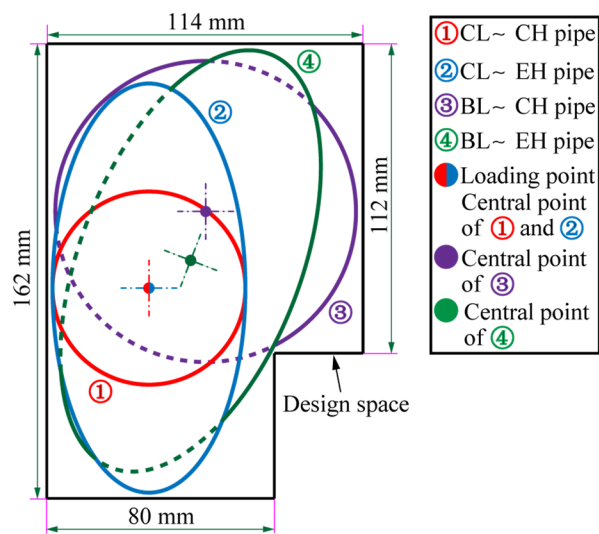
Figure 21. The envelope of four types of pipes in the same design space. (① is the circular-helical pipe with center loading, ② is the elliptical-helical pipe with center loading, ③ is the circular-helical pipe with bias loading, ④ is the elliptical-helical pipe with bias loading, the half red and half blue point is the loading point of pipes ①–④ and the center point of pipes ① and ②; the purple point is the center point of pipe ③; the green point is the center point of pipe ④; and pipes ①–④ are in the optimal configuration for axial stiffness of each type of pipe in this design space).

Table 5. Parameters of four types of pipes.

Variable/Pipe Number	①	②	③	④
a/mm	32	70	53	78
b/mm	32	32	53	39
$P\,(m, n)$/mm	$(0, 0)$	$(0, 0)$	$(20, -28)$	$(-13.4, -8.6)$
N/turns		4		
λ [1]/mm		27		
K/(N/mm)	1.09	0.27	0.24	0.18
F [2]/N	29.43	7.29	6.48	4.86
σ_{max} [3]/MPa	172.06	94.05	103.44	81.41

[1] λ represents the stretched length of the refueling pipe (half of the docking distance); [2] F represents the force stretching the pipe by the length λ; [3] σ_{max} represents the maximum stress of the refueling pipe subjected to force F.

Table 6. Parameters of the matched spring pins.

Spring Pins/Pipe Number		①	②	③	④
Linear	$F_{s3,4}$ [1]/N	5.52	2.30	2.30	1.84
	$K_{s3,4}$ [2]/(N/mm)	0.46	0.46	0.46	0.46
Pitch	F_{s1}/N	2.25	1.50	11.50	3.00
	K_{s1}/(N/mm)	0.75	0.75	2.30	0.75
Yaw	F_{s2}/N	2.25	1.50	9.20	3.00
	K_{s2}/(N/mm)	0.75	0.75	2.30	0.75
Roll	F_{s5}/N	6.60	2.16	2.16	2.16
	K_{s5}/(N/mm)	1.10	0.36	0.36	0.36

[1] F_s represent the preloading of the spring pins; [2] K_s represent the axial stiffness of the spring pins.

In this section, two types of dynamic simulations (contact force and driving force) were performed for four types of pipes (using the optimal configuration of axial stiffness for each type) and the corresponding pairs of spring pins. The simulation of the contact force is intended to verify the validity of the dynamic models. The simulation of the driving

force is thus to show the superiority of the configuration using the elliptical-helical pipe. The 3D model is the same as that used in the kinematic simulation.

For the simulations of contact force, four types of working conditions are sufficient to verify the validity of the dynamic model, including three typical decoupling conditions, (X -2 mm), (Roll $-1°$), (Yaw $-1°$), and one typical coupling condition, (X -2 mm, Roll $-1°$, Yaw $-1°$). Then, corresponding experiments were performed to validate the results of the simulations. The dynamic experimental system is the same as that used in the kinematic experiment system, as shown in Figure 19. A six-component force sensor installed at the root of the probe is used to detect contact forces. The key positions of the docking are shown in Figure 22, used to support dynamic results.
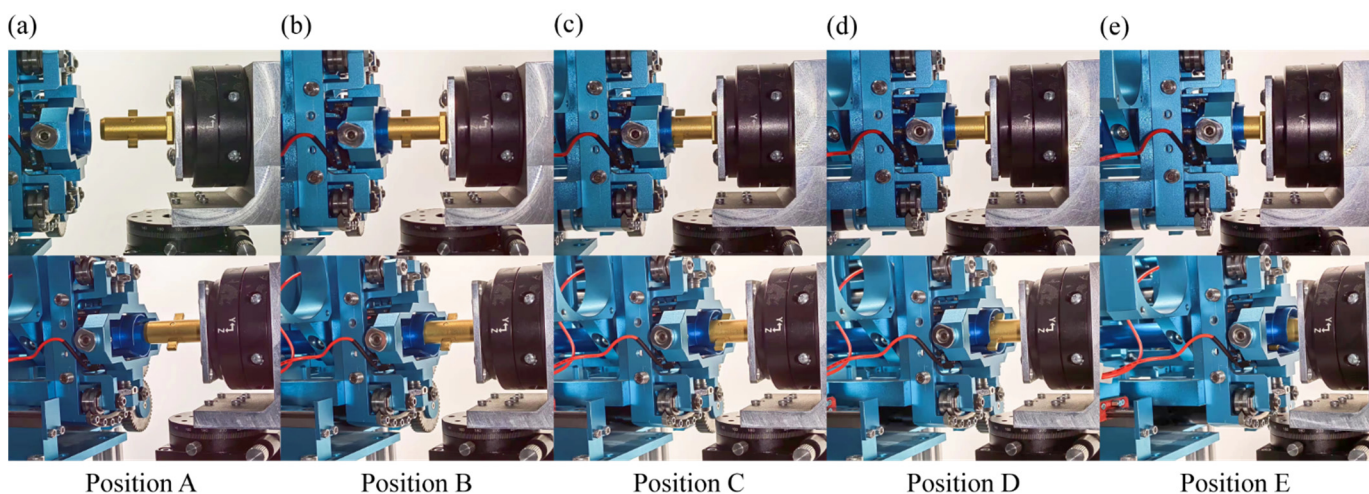

Figure 22. Key positions of the docking: (**a**) Position A—Initial, (**b**) Position B—Contact and alignment I, (**c**) Position C—Probe insertion and alignment II, (**d**) Position D—Pin insertion and alignment III, (**e**) Position E—Accomplishing. (The explanation of position A—E can be found in Section 2.2.)

The results of the contact force simulations and experiments are shown in Figure 23. Four types of working condition are setting, which can cover the whole docking conditions. The points worth noticing are points B, C, and D, which are the turning points of docking state. The curve worth noticing is F_y, which is the contact force of the docking direction and influence the driving force directly. As shown in Figure 23, the trends (especially curve F_y) and most of the values (especially points C and D) of the experiment curves can correspond by the simulation curves. In view of machining errors, sensor accuracy and the estimation of friction coefficient, the agreements between simulations and experiments are more than 70% and the key points and curves are more than 85%, which reciprocally verifies the validity of the simulations and experiments. Therefore, the driving forces of the mechanism with four types of pipes above can be obtained from the simulations instead of experiments, which can save time and resources, to verify the superiority of the proposed elliptical-helical refueling pipe and meet the requirement R3 in Section 2. The results of the driving force are shown in Figure 24. The working conditions for driving force verification are the typical coupling conditions of (X -2 mm, Z -2 mm, Roll $-1°$, Yaw $-1°$, Pitch $-1°$). The results show that both the envelope and the maximum value of driving force of the mechanism with the elliptical-helical pipe are optimal, where the elliptical-helical pipe with center loading has 40% reduction compared with the circular-helical pipe with center loading, which verifies the superiority of the elliptical-helical refueling pipe for on-orbit berthing-based refueling.
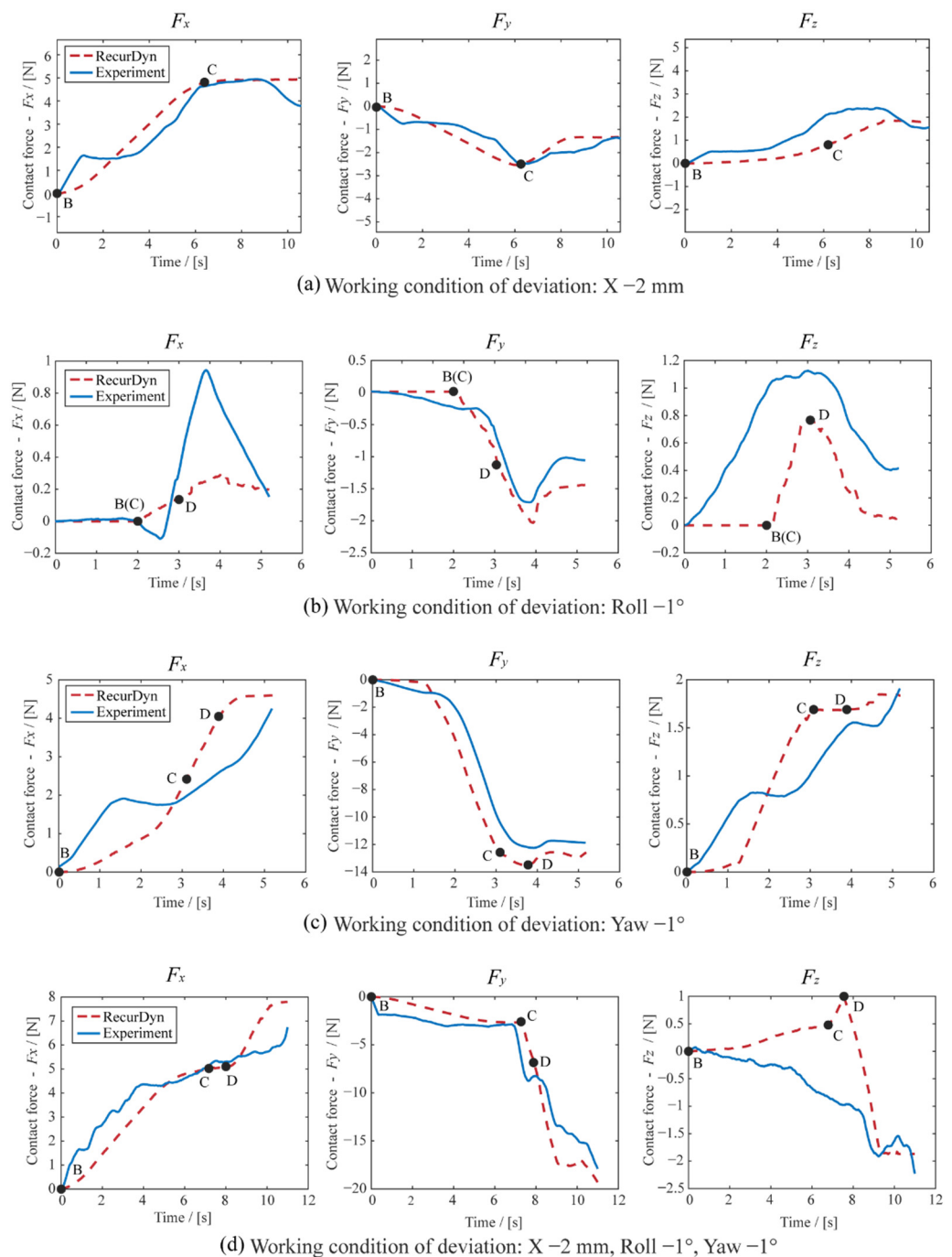
(a) Working condition of deviation: X −2 mm

(b) Working condition of deviation: Roll −1°

(c) Working condition of deviation: Yaw −1°

(d) Working condition of deviation: X −2 mm, Roll −1°, Yaw −1°

Figure 23. Results of contact forces by simulation and experiment: (**a**) (X −2 mm), (**b**) (Roll −1°), (**c**) (Yaw −1°), (**d**) (X −2 mm, Roll −1°, Yaw −1°). The three subplots of each condition are the curve of component forces of contact force, *Fx*, *Fy*, and *Fz* and time, from left to right; the points B, C, and D represent the corresponding key positions of docking in Figure 22.
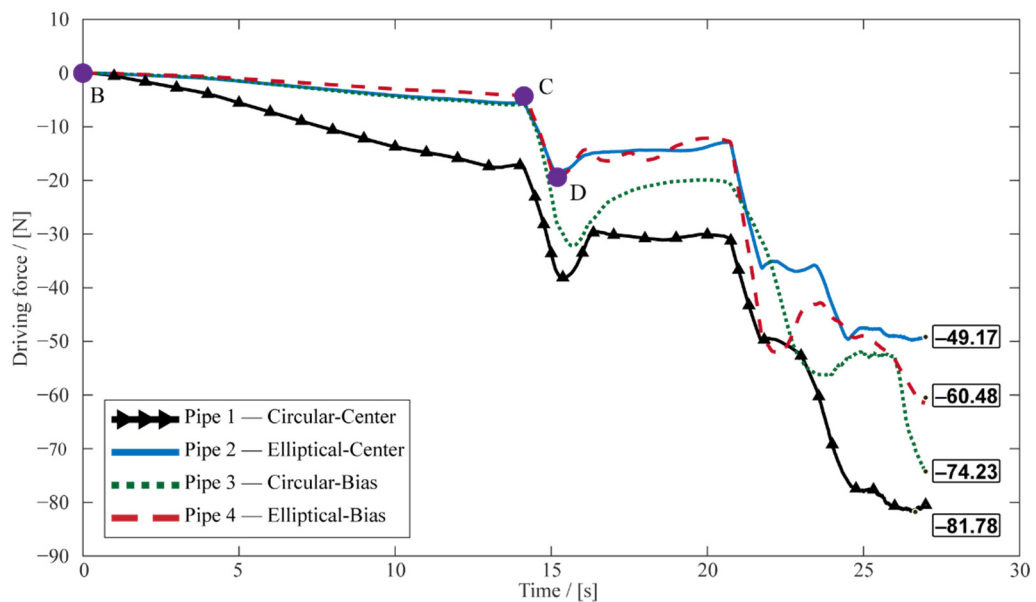
Figure 24. Results of driving forces by simulation: (X −2 mm, Z −2 mm, Roll −1°, Yaw −1°, Pitch −1°). The maximal driving forces (listed from pipe 1 to pipe 4) are 49.17 N, −60.48 N, −74.23 N, and −81.78 N. (The definitions of the points B, C and D can be found in Figure 22.)

5. Conclusions

This paper proposes a novel floating docking mechanism for on-orbit refueling during berthing, and the design details are described exhaustively. A probe–drogue configuration is adopted for the proposed mechanism to achieve passive alignment and self-resetting for five DOFs. Two double-winding servo motors are equipped with a redundancy design to increase docking reliability. The proposed mechanism is light, compact, and simple, aiming to achieve a lower driving force. Considering the characteristics of berthing docking, mechanical analysis of the docking process, and the compactness required for on-orbit mechanisms, an elliptical-helical pipe with bias loading is proposed to decrease the requirement of the driving force. The formula for axial stiffness is derived using the energy-based method, and strength checking is derived using the third strength theory.

To verify the validity of the proposed model and method, three types of simulations and experiments were performed: static analysis of the mechanical properties of the refueling pipe, kinematic analysis of the tolerance range of the docking mechanism, and dynamic analysis of the driving force of the docking mechanism. For the static analysis, the relative error of the axial stiffness and maximum stress of the theoretical resolution and simulation are less than 1.2% and 0.6%, respectively, and the relative error of the axial stiffness of the theoretical and experimental result is less than 4.4%, which verifies the accuracy of the formula of axial stiffness. For the kinematic analysis, the results of the simulations and experiments verify the correctness of the estimated tolerance range with values of ±4 mm on two linear misalignments and ±2.5° on three angular misalignments and the self-resetting ability, which meet R1 and R2 in Section 2. For the dynamic analysis, all trends and values of the contact force under four typical working conditions obtained by the simulations coincide with the experiments, which verifies the validity of the dynamic simulation model. Then, the dynamic simulation model obtains the driving forces of the docking mechanism with four types of pipes (circular-helical or elliptical-helical pipe with center loading or bias loading). Both the envelope and the maximum driving force of the mechanism with the elliptical-helical pipe are superior to those of the circular-helical pipe, which is suitable for the proposed docking mechanism, meeting R3 in Section 2.

Author Contributions: Conceptualization, Z.S., S.L. and X.S.; Methodology, Z.S. and H.Z.; Software, Z.S. and H.L.; Validation, Z.S. and H.L.; Formal analysis, Z.S., S.L. and X.S.; Investigation, Z.S.;

Institutional Review Board Statement: Not applicable.

Informed Consent Statement: Not applicable.

Data Availability Statement: Not applicable.

References

1. Li, W.; Cheng, D.; Liu, X.; Wang, Y.; Shi, W.; Tang, Z.; Gao, F.; Zeng, F.; Chai, H.; Luo, W.; et al. On-orbit service (OOS) of spacecraft: A review of engineering developments. *Prog. Aerosp. Sci.* **2019**, *108*, 32–120. [CrossRef]
2. Barbara, N.H.; Lizy-Destrez, S.; Guardabasso, P.; Alary, D. New GEO paradigm: Repurposing satellite components from the GEO graveyard. *Acta Astronaut.* **2010**, *173*, 155–163. [CrossRef]
3. Chato, D.J. Technologies for refueling spacecraft on-orbit. In Proceedings of the AIAA Space 2000 Conference and Exposition, Long Beach, CA, USA, 19–21 September 2000. [CrossRef]
4. Meng, B.; Huang, J.; Li, Z.; Huang, L.; Pang, Y.; Han, X.; Zhang, Z. The orbit deployment strategy of OOS system for refueling near-earth orbit satellites. *Acta Astronaut.* **2019**, *159*, 486–498. [CrossRef]
5. Zhu, X.; Zhang, C.; Sun, R.; Chen, J.; Wan, X. Orbit determination for fuel station in multiple SSO spacecraft refueling considering the J2 perturbation. *Aerosp. Sci. Technol.* **2020**, *105*, 105994. [CrossRef]
6. Chen, X.; Yu, J. Optimal mission planning of GEO on-orbit refueling in mixed strategy. *Acta Astronaut.* **2017**, *133*, 63–72. [CrossRef]
7. Zhou, Y.; Yan, Y.; Huang, X.; Kong, L. Optimal scheduling of multiple geosynchronous satellites refueling based on a hybrid particle swarm optimizer. *Aerosp. Sci. Technol.* **2015**, *47*, 125–134. [CrossRef]
8. Pan, G.; Jia, Q.; Chen, G.; Li, T.; Liu, C. A control method of space manipulator for peg-in-hole assembly task considering equivalent stiffness optimization. *Aerospace* **2021**, *8*, 310. [CrossRef]
9. Huang, P.; Wang, M.; Meng, Z.; Zhang, F.; Liu, Z. Attitude takeover control for post-capture of target spacecraft using space robot. *Aerosp. Sci. Technol.* **2016**, *51*, 171–180. [CrossRef]
10. Li, Y.; Li, D.; Zhu, W.; Sun, j.; Zhang, X.; Li, S. Constrained motion planning of 7-DOF space manipulator via deep reinforcement learning combined with artificial potential field. *Aerospace* **2022**, *9*, 163. [CrossRef]
11. Shan, M.; Shi, L. Comparison of tethered post-capture system models for space debris removal. *Aerospace* **2022**, *9*, 33. [CrossRef]
12. Yang, H. *Manned Spacecraft Technologies*; Beijing Institute of Technology Press: Beijing, China, 2021.
13. Cislaghi, M.; Santini, C. The Russian docking system and the automated transfer vehicle: A safe integrated concept. In Proceedings of the 3rd IAASS Conference Building a Safe Space Together, Rome, Italy, 21–23 October 2008.
14. Motaghedi, P. On-orbit performance of the Orbital Express Capture System. In Proceedings of the SPIE Defense and Security Symposium, Orlando, FL, USA, 16 March 2008. [CrossRef]
15. Medina, A.; Tomassini, A.; Suatoni, M.; Aviles, M.; Solway, N.; Coxhill, I.; Paraskevas, I.; Rekleitis, G.; Papadopoulos, E.; Krenn, R.; et al. Towards a standardized grasping and refueling on-orbit servicing for GEO spacecraft. *Acta Astronaut.* **2017**, *134*, 1–10. [CrossRef]
16. Vedova, F.D.; Morin, P.; Roux, T.; Brombin, R.; Piccinini, A.; Ramsden, N. Interfacing sail modules for use with "Space Tugs". *Aerospace* **2018**, *5*, 48. [CrossRef]
17. Javier, V.; Guerra, G. Standard interface for robotic manipulator (SIROM): SRC H2020 OG5 final results-future upgrades and applications. In Proceedings of the International Symposium on Artificial Intelligence, Robotics and Automation in Space (i-SAIRAS), Virtual, 19–23 October 2020.
18. Coll, G.T.; Webster, G.K.; Pankiewicz, O.K.; Schlee, K.L.; Aranyos, T.J.; Nufer, B.M.; Fothergill, J.; Tamasy, G.; Kandula, M.; Amy, F.; et al. NASA's exploration and In-Space services (NExIS) division OSAM-1 propellant transfer subsystem progress 2020. In Proceedings of the AIAA Propulsion and Energy 2020 Forum, Las Vegas, NV, USA, 24–26 October 2020.
19. Phisannupawong, T.; Kamsing, P.; Torteeka, P.; Channumsin, S.; Sawangwit, U.; Hematulin, W.; Tanatthep, J.; Somjit, T.; Yooyen, S.; Delahaye, D.; et al. Vision-based spacecraft pose estimation via a deep convolutional neural network for noncooperative docking operations. *Aerospace* **2020**, *7*, 126. [CrossRef]
20. Lazzarin, M.; Biolo, M.; Bettella, A.; Manente, M.; Da Forno, R.; Pavarin, D. EUCLID satellite: Sloshing model development through computational fluid dynamics. *Aerosp. Sci. Technol.* **2014**, *36*, 44–54. [CrossRef]
21. Cook, J.; Aksamentov, V.; Hoffman, T. ISS interface mechanisms and their heritage. In Proceedings of the AIAA Space 2011 Conference & Exposition, Long Beach, CA, USA, 27–29 September 2011. [CrossRef]
22. Underwood, C.; Pellegrino, S.; Lappas, V.J.; Bridges, C.P.; Baker, J. Using CubeSat/micro-satellite technology to demonstrate the Autonomous Assembly of a Reconfigurable Space Telescope (AAReST). *Acta Astronaut.* **2015**, *114*, 112–122. [CrossRef]

23. Hays, A.B.; Tchoryk, P.; Pavlich, J.C.; Ritter, G.A.; Wassick, G.J. Advancements in design of an autonomous satellite docking system. In Proceedings of the Defense and Security Symposium, Orlando, FL, USA, 12 April 2004. [CrossRef]

24. Boesso, A.; Francesconi, A. ARCADE small-scale docking mechanism for micro-satellites. *Acta Astronaut.* **2013**, *86*, 77–87. [CrossRef]

25. Branz, F.; Olivieri, L.; Sansone, F.; Francesconi, A. Miniature docking mechanism for CubeSats. *Acta Astronaut.* **2020**, *176*, 510–519. [CrossRef]

26. Xavier, C.; Sun-Wook, K.; Michel, I.; Arun, M.; Gilbert, J. Post-impact dynamics of two multi-body systems attempting docking/berthing. *Acta Astronaut.* **1997**, *40*, 759–769. [CrossRef]

27. Dunn, B.D. *Materials and Processes for Spacecraft and High Reliability Applications*; Springer: Berlin/Heidelberg, Germany, 2016.

28. Dym, C.L. Consistent derivations of spring rates for helical springs. *ASME J. Mech. Des.* **2009**, *131*, 071004. [CrossRef]

29. Spinella, I.; Dragoni, E. Modeling, prototyping, and testing of helical shape memory compression springs with hollow cross section. *ASME J. Mech. Des.* **2010**, *132*, 061008. [CrossRef]

30. Jafari, M.; Mahjoob, M.J. An exact three-dimensional beam element with nonuniform cross section. *ASME J. Appl. Mech.* **2010**, *77*, 3214–3220. [CrossRef]

31. Burns, S.J. The relation between helical spring compliances with free and fixed end rotations. *ASME J. Appl. Mech.* **2011**, *78*, 61005. [CrossRef]

32. Liu, H. *Mechanics of Materials I*, 4th ed.; Higher Education Press: Beijing, China, 2007. (In Chinese)